Coherent Anti-Stokes Raman Spectroscopy Measurements of Temperature Fluctuations in Turbulent Natural Gas-Fueled Piloted Jet Diffusion Flames

JOHN MANTZARAS* AND THEO H. VAN DER MEER

Delft University of Technology, Department of Applied Physics, Heat Transfer Section, Lorentzweg 1, Delft 2628-CJ, The Netherlands

Temperature fluctuations have been measured in a turbulent, natural gas-fueled, piloted jet diffusion flame with a fuel jet exit Reynolds number of 9700, using broadband Coherent Anti-Stokes Raman Spectroscopy (CARS) nitrogen thermometry with a best spatial resolution of 0.9 mm. Radial profiles of mean temperature and root mean square (rms) temperature fluctuations have been acquired and temperature probability density functions (pdfs) have been constructed for streamwise distances in the range $4.2 \leq x/d \leq 66.7$. Comparison with thermocouple measurements shows very good agreement (within 50 K) in regions of moderate temperature gradients (jet core and jet tails), whereas in the steeper gradient jet flank areas spatial averaging leads to CARS mean temperatures lower by as much as 60 K for $x/d \geq 25$ and by 150 K for $x/d = 8.3$. The largest rms temperature fluctuations (640 K) occur at radial locations corresponding to about 70% of the full jet height, for all streamwise distances. Comparison with numerical predictions that employ a k-ε model for turbulence and a constrained equilibrium model for chemistry along with a presumed pdf shape (β function) for the mixture fraction, shows very good agreement, for $x/d \geq 16.7$, between computed and measured peak and centerline mean temperatures and rms temperature fluctuations, and fair agreement for $x/d = 8.3$. The thermal jet widths are underpredicted for $x/d \geq 25$. Measured pdfs attain a variety of shapes, from nearly symmetric around the centerline and bimodal near the average reaction zone location, to nearly uniform in parts of the jet flanks and, finally, to triangular at the jet tails. In addition, measured centerline pdfs evolve from triangular to nearly Gaussian as x/d increases. The agreement between predicted and measured pdf shapes is excellent at the centerline and is very good in other parts of the jet flame, with the possible exception of bimodal shapes around the average reaction zone location, attributed to inherent limitations in the beta function representation.

INTRODUCTION

In nonpremixed turbulent combustion there is great interest in thoroughly understanding combustion in simple geometrical configurations such as axisymmetric turbulent diffusion flames. This is a necessary first step toward the ultimate goal of designing more efficient and cleaner industrial combustion devices, the vast majority of which operate with nonpremixed reactants. In the last 15 years there has been a rapid growth in laser diagnostic techniques for the nonintrusive probing of jet diffusion flames. Crucial in the development of these techniques was the introduction of simultaneous spatially and temporally resolved measurements of a number of scalars [1–6]. This was followed by recent planar temporally resolved simultaneous measurements of a smaller number of scalars [7–9]. Such simultaneous measurements are crucial for nonpremixed combustion, where the mixture fraction and the scalar dissipation rate play a key role. The measurement of major combustion species along with combustion intermediates (notably CO) and radicals as well as temperature, have enhanced the understanding of the structure of turbulent nonpremixed flames. This is particularly important in processes controlled by finite rate kinetics such as near extinction conditions [1–3], formation of NO [5], formation and burnout of CO [1, 2], and stabilization mechanisms in lifted hydrocarbon flames [4, 8]. Except for [6], all previous studies have employed a combination of Raman and Rayleigh scattering for the measurement of major species and temperature. This approach, however, requires the composition of the fuel stream to be tailored to reduce interference of soot precursors

* Corresponding author. Present address: Paul Scherrer Institute, Combustion Research, CH-5232 Villigen PSI, Switzerland.

COMBUSTION AND FLAME 110: 39–53

Published by Elsevier Science Inc.

0010-2180/97/$17.00
PII S0010-2180(97)00070-9

with the Raman signal and minimize variations in the Rayleigh scattering cross section area across the flame. This has led to the use of either nonluminous hydrogen–air flames or highly diluted hydrocarbon flames.

Although much has been gained on the fundamentals of nonpremixed combustion from the previous studies, information is still needed on the combustion of realistic fuels such as undiluted methane or commercially available natural gas—a need further accentuated by the current trend toward the use of alternative, heavier and less clean fuels. In these cases both NO formation and the formation and burnout of CO and soot occur primarily in the higher-temperature, luminous regions where combined Raman–Rayleigh scattering have limited or no applicability. The present paper reports a detailed mapping of the fluctuating temperature field in a jet flame with a fuel jet exit Reynolds number of 9700 for streamwise distances spanning from the lower blue zone to the middle luminous zone. For nonintrusive accurate temperature measurements in particle-laden flames, Coherent Anti-Stokes Raman Spectroscopy (CARS) is the best suited approach, albeit with some added complexity, and was employed in this study. It is a four-wave mixing technique [10, 11] and has been successfully aplplied in the hostile environments of many practical combustors with a typical accuracy of ± 50 K. CARS enjoys the advantage of a coherent and hence highly directional laser-like signal with very high conversion efficiency, several orders of magnitude stronger than spontaneous Raman [11], and hence it strongly discriminates against laser-induced background interferences.

Point temperature probability density functions (pdf) measured with Raman–Rayleigh scattering have been reported in clean turbulent jet diffusion flames, for example, in a CH_4/H_2 flame at a streamwise distance of $x/d = 65$ [12], at the base of a natural gas lifted flame with a Reynolds number of 28,600 [4], or at the base of lifted CH_4 flames with Reynolds numbers of 7000 and 12,100 [8]; in the blue parts of CH_4 flames at four different Reynolds numbers and at three streamwise distances [2]; in a highly diluted CH_4 flame with a Reynolds number of 20,600, at $x/d = 25$ [9]; and, finally, in a hydrogen flame (Re = 8500) at $x/d = 50$ [13]. CARS temperature pdfs have been presented for two Reynolds numbers (6000 and 2000) propane flames and five streamwise locations [14]. In [6], CARS temperature pdfs are presented, conditioned to simultaneous velocity measurement for a propane–air mixture at Re = 4000 and three streamwise locations. Comparison of measured and numerically predicted temperature pdf shapes has not been elaborated in previous studies. The present paper reports such comparisons.

The experimental configuration and flow conditions are first given, along with some earlier measurements that help to delineate the regime(s) of turbulent combustion for our flame. A brief description of the mathematical model then follows, and the results are presented. Comparison is first made with thermocouple measurements and then with numerical predictions. Initially we compare radial profiles of mean temperature and root mean square (rms) temperature fluctuations. A detailed comparison then follows between measured and predicted temperature pdf shapes, initiating a discussion on characteristics of the flame such as flame strain, extinction, turbulent mixing, and intermittency.

EXPERIMENTAL APPROACH

Burner Configuration and Flow Conditions

The burner is depicted in Fig. 1 and consists of two vertical, 1-m-long concentric tubes, with the central tube providing the fuel and the annular region providing the primary air. Near the burner nozzle the inner surface of the annulus becomes conical with a contraction angle of 7°, leading to an inner annulus diameter of 15 mm at the burner rim. The outer lips of the annulus are thin. The inner lips, however, maintain a thickness of 4.5 mm to accommodate a pilot flame insert. Behind the thick inner lip areas a small recirculation zone is established, providing an additional stabilization mechanism apart from that of the pilot flames. The pilot flame insert ends in a ring-shaped disk with a 6-mm internal diameter (d). Pilot flames are located on 12 0.5-mm-

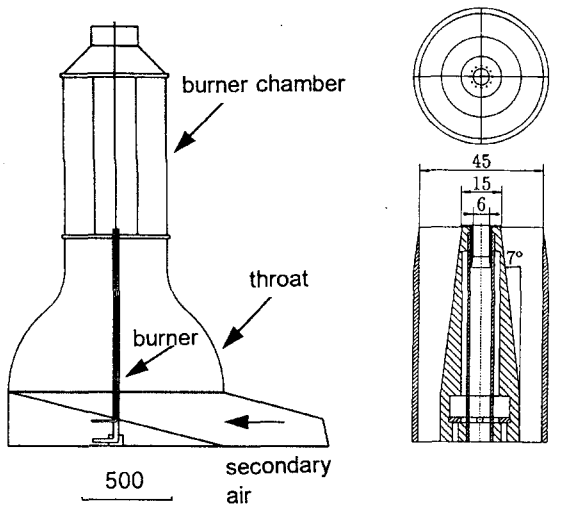

Fig. 1. Burner, burner throat and chamber, and details of the burner nozzle. All distances in millimeters.

diameter holes arranged on the 7-mm diameter of the disk. The burner is centered in a coflowing secondary air stream that flows first along a ramp, a flow straightening blanket, and then through a throat. At the test section entrance the throat attains an octagonal cross section to approximate the circular walls used in the numerical simulations. An octagonal combustion chamber 0.9 m high and 0.57 m wide with optical access from all sides is located in the test section. At the test section entrance the secondary air flow velocity is 0.3 m/s with very low turbulence. The fuel was commercially available Dutch natural gas with a molar composition of 81.3% CH_4, 2.9% C_2H_6, and 14.3% N_2. The mixture for the pilot flames consisted of acetylene–hydrogen–air with a C/H ratio equal to that of the natural gas, as in Stårner and Bilger [15], and their heat release was 1% of the total flame. The main fuel gas velocity was 21.9 m/s and the primary air velocity was 4.4 m/s, resulting in Reynolds numbers for the fuel jet and primary air jet of 9700 and 8800, respectively, and a flame power of 20 kW. The fuel/air ratio corresponds to a primary air excess of 18%. The visible flame length is 0.85 m and the visibly soot-free flame length is approximately 0.2 m.

For the three-flow system described in the foregoing text, two shear layers develop—an inner one between the fuel jet and primary air flow and an outer one between the primary and secondary air flows. The inner shear layer is an important source of turbulence because of the large velocity excess of the two streams. For high CH_4 content of the fuel, the stoichiometric mixture fraction (ξ) attains a low value of 0.07. This places the reaction zone, at least for small streamwise distances, outside the surface of the strongest shear stresses and close to the outer boundary of the inner shear layer. As x/d increases, the average stoichiometric surface ($\xi_{st} = 0.07$) approaches the inner shear layer and coincides with it at $x/d \approx 45$. For streamwise distances $x/d > 30$, Planar Laser Induced Fluorescence (PLIF) measurements of OH [16] suggest that turbulent eddies have grown sufficiently to entrain secondary quiescent flow at the mean stoichiometric surface location. Figure 2 is a plot of the measured, in an identical burner, centerline axial (u') and radial (v') turbulent velocities and turbulent kinetic energy (k) versus x/d, from [17]. On the same figure, indirect measurements (invoking Taylor's hypothesis) of the longitudinal axial integral length scale (L) also are given. The region $10 < x/d < 33$ has the highest turbulent kinetic energy and the smallest length scale of the jet flame, leading to the highest strain rates. According to Peters' classification of regimes of turbulent nonpremixed combustion [18], a distributed reaction zone is encountered near the burner nozzle and further downstream a small part of the flame lies in the extinguishing flamelet regime, whereas the

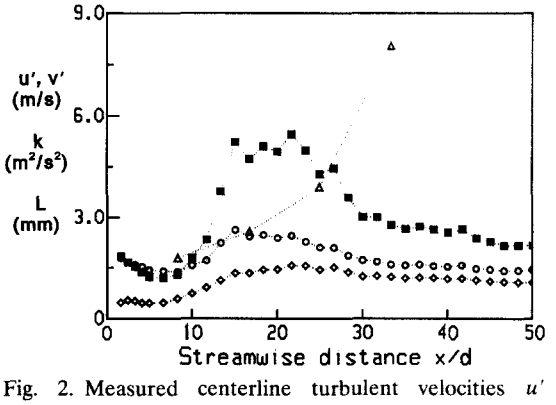

Fig. 2. Measured centerline turbulent velocities u' (circles), v' (diamonds), turbulent kinetic energy k (divided boxes), and longitudinal axial integral length scale L (triangles) from [17].

remaining main part lies in the flamelet regime. This classification is further supported by experimental evidence of frequent local extinction (manifested from the existence of holes in the PLIF-measured OH structure [16]) in the intensely strained region extending from $x/d \approx 7$ to ≈ 25. Measurements were performed in the higher strain rate and extinguishing regions, $4.2 \leq x/d \leq 66.7$.

Optical System

The CARS configuration (Fig. 3) consists of a frequency-doubled Nd:YAG laser (Continuum YG-680) operating at 10 Hz with a typical pulse duration of 6 ns, yielding 350 mJ per pulse at $\lambda_1 = 532$ nm. The laser is multimode pumped, resulting in a ω_1 linewidth of 1 cm^{-1}. Eighty percent of the ω_1 radiation is split off to pump a broadband oscillator–amplifier dye laser (Continuum TDL-60). The resulting Stokes radiation (ω_2) has a bandwidth of 150 cm^{-1} full width at half maximum and its central wavelength is tuned to 607 nm by adjusting the dye concentration (rhodamine 640). The remaining 20% of the pump radiation is split off to form two equal intensity pump beams. The Stokes and the two pump beams are focused inside the combustion chamber by a 350-mm focal length lens. A folded BOXCARS phase-matching scheme is used for best resolution and ease of CARS signal separation [19]. The resulting CARS radiation ($\omega_3 = 2\omega_1 - \omega_2$) is recollimated, spectrally dispersed in a SPEX-1404 0.85-m double spectrometer, and recorded on a gated intensified photodiode array (IPDA) detector of 1024 diodes (Princeton Instruments IRY-1024) with a 14-bit dynamic range. In constant pressure combustion peak CARS intensities can decrease by a factor of 10^3 between room and flame temperature. To increase the dynamic range of the detector, a beam splitter splits the total CARS signal in two, with an intensity ratio of 10:1. Both CARS signals are then spectrally dispersed on the spectrometer, which operates slitless, and recorded simultaneously on the spectral field of the array detector. The corresponding spectral dispersion is 0.3 cm^{-1} per diode and the spectral resolution of the recorded CARS spectra is about 1.5 cm^{-1}. The active, CARS spectra containing diodes of the array are digitized and stored in a dedicated Pentium-based PC with 1.3-Gbyte memory for later processing. The spatial resolution plays an important role in CARS thermometry of laboratory scale turbulent flames with steep temperature gradients, and therefore its strict definition should be used [20]. The pump and Stokes beam diameters are expanded to 10 mm with Galilean telescopes, and the beam half crossing angle is set to 2.45°. The resulting interaction length (95% of the total CARS energy) was measured as 900 μm by traversing a thin quartz plate across the CARS probe volume.

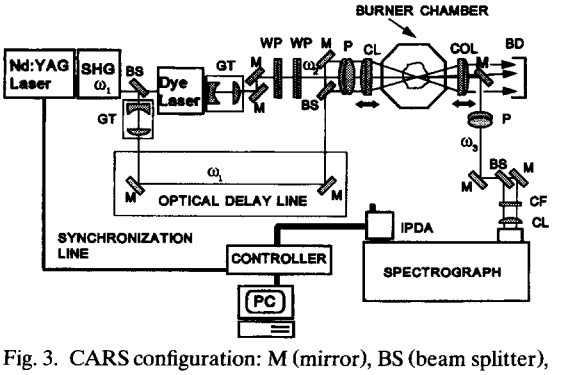

Fig. 3. CARS configuration: M (mirror), BS (beam splitter), WP (wedge prism), P (periscope), CL (condensing lens), COL (collimating lens), CF (cutoff filter), GT (Galilean telescope), BD (beam dump).

Evaluation of Precision and Accuracy

The main systematic errors arise from the response characteristics of the IPDA detector, the long term dye laser spectral shift, spatial averaging effects in areas of steep temperature gradients, and the accuracy of knowing the experimental parameters in the CARS code fitting process. Each of these effects is discussed subsequently. Nonlinearity and image persistence is known to be a serious problem in IPDA detectors incorporating earlier phosphor-based intensifiers [21]; both effects result in low temperature bias. To eliminate these problems the intensifier was refitted with a fast P-43 type phosphor. One cleansing scan between laser shots was sufficient, for the 10-Hz operational frequency, to reduce image persistence to less than 0.04% of the previous expo-

sure signal level. The linearity response of the detector was checked with single-element calibrated neutral density filters and room temperature CARS spectra at a fixed gain setting. The detector sensitivity was found to be constant in the range of 15–10,000 counts. Hence, neither IPDA related response characteristic contributes significantly to lower temperature bias. Dye profile spectral shift in long-lasting experimental runs was found to present a problem. To minimize this effect, an initial fast radial scan of the CARS optics was performed and acquired 1000 measurements at each radial location, which are sufficient to reproduce the mean temperature and its rms fluctuations. Later, at selected radial locations, 5000 measurements were taken to obtain detailed statistics. Data reduction with nonresonant reference spectra acquired before and after the experiment showed that the dye spectral shift effect contributes ± 30 K uncertainty to the mean deduced temperature in the hot parts ($T > 1000$ K) of the flame.

A main source of error is spatial averaging [22], which biases the temperature to lower values; this problem is compounded with the highly nonlinear nature of the biasing. It becomes particularly important in the steep temperature gradient parts near the reaction zone of the flame. PLIF measurements [16] indicate instantaneous OH thicknesses of 1.13 ± 0.15 and 1.70 ± 0.5 mm at streamwise locations $x/d = 8.3$ and 50, respectively, where most of the present measurements lie. Furthermore, the reaction zone itself is expected to be even thinner than the OH thickness suggests. Such steep gradients cannot be resolved even with the nominal spatial resolution of 0.9 mm for CARS. However, when constructing temperature pdfs in turbulent flames, the key element is the probability of the CARS volume containing the steepest reaction zone gradients; if this probability is low, which is the case in our strongly fluctuating flame, the resulting distributions are largely unaffected. At $x/d = 8.3$ and in the outer, air-rich hot parts of the jet wings ($T > 800$ K) a mean temperature underestimate of about 130 K is to be expected. For $x/d \geq 25$, this underestimate can be as low as 60 K. As will be discussed, at the lowest streamwise location $x/d = 4.2$ the gradients are sufficiently steep to alter significantly the temperature distributions, except near the centerline.

The precision of CARS-deduced temperatures depends also on how accurately experimental parameters such as nonresonant susceptibility, slit width, and spectral dispersion are known. A major problem in diffusion flames is the large nonresonant susceptibility (χ_{nr}) in the fuel-rich parts of the flame. A two-parameter fit (temperature and the ratio of the probed species mole fraction to the average molecular background susceptibility) is then essential to avoid substantial temperature overestimate [23]. With a two-parameter fit, the inferred temperature is largely unaffected by the initial value of the unknown instantaneous background susceptibility or composition, as long as there is a sufficient resonant signal. In our flame a minimum 14.3% mole fraction for the resonant nitrogen species is assured at all locations. An additional complication arises in the fuel-rich core of the flame with the standard convolution of CARS spectra. The standard convolution was found [22] to give slightly higher temperatures in regions of large nonresonant background and when the pump laser linewidth was much greater than the Raman linewidth of the probed molecule, as is the case with the multimode pumped laser. We also observed somewhat higher mean temperatures (by about 30 K) in the fuel-rich core of the flame, compared with thermocouple measurements, and this is attributed to this effect. Finally, in sooty flames and when the pump is the frequency-doubled Nd:YAG radiation, absorption in the fundamental band of the CARS radiation by C_2 (formed by laser vaporization of soot particles) can cause substantial temperature overestimate when fitting the entire CARS spectrum is attempted. The small soot volume fraction of the flame (1.5×10^{-8}) measured with a suction probe does not pose a serious problem. In [24] a minimum soot volume fraction of 10^{-6} is judged important for C_2 absorption related problems.

Random errors are mainly shot-to-shot dye spectral fluctuations. They were assessed by calibrating in the 1500–1850-K temperature range, across a lean ($\Phi = 0.84$) CH_4–air premixed laminar flat flame with postflame gas

radiation heat losses. Measured mean temperatures were within 25 K of the numerical predictions and the rms fluctuations were about 50 K. The random error of 50 K has a minimal effect on the measured pdf shapes, particularly in the hot parts of the flame where large temperature fluctuations (up to 640 K) are present. The random error at room temperature can be as high as 20 K. It can therefore become the most important source of error for the jet tails, where very low fluctuations are encountered around an almost room temperature mean. Finally, beam steering could cause measurement rejections (and hence a temperature bias) whenever beam overlap is not attained in the CARS volume. This problem was not present in this study due to the small optical path lengths.

The computer code used for the spectra fit was DACAPO [25]. Four parameters were fitted: the temperature, the ratio of concentration to nonresonant susceptibility, a frequency stretch factor, and a frequency shift factor. A least-squares fit method was used for the normalized measured spectra. An indicator of the fitting error for each spectrum was the rms deviation $\sigma = [\sum_{i=1}^{N}(I_i - I_{c,i})^2/(N-1)]^{0.5}$, where I_i and $I_{c,i}$ are the intensities of the measured and calculated spectra, respectively, and N is the number of diodes per spectrum. Requiring $\sigma < 0.05$, acceptances were about 95%. The fitting errors did not correlate with the values of the temperature, but rather with the values of the nonresonant susceptibility. At the jet core of the lowest streamwise location $x/d = 8.3$, the acceptance was somewhat lower (90%).

Overall, we estimate the combined uncertainty for the deduced mean temperatures to be about +30 K/− 70 K in the fuel-rich part of the flame between the average reaction zone locations (further referred to as the jet core); to +40 K/− 20 K in the low temperature ($T < 600$ K) parts of the air-rich wings of the jet flame (further referred to as jet flanks) for $x/d \geq 16.7$, and +80 K/− 0 K at $x/d = 8.3$; to +160 K/− 0 K for the steep gradient high temperature regions ($T > 800$ K) of the jet flanks at $x/d = 8.3$. At the higher streamwise locations the last uncertainty can be as low as +80 K/− 0 K.

NUMERICAL APPROACH

The mathematical model [16] is based on Favre-averaged transport equations for mass, momentum, and energy in cylindrical coordinates. For turbulence, a first order closure is employed with a standard k-ε model supplemented with a correction for round-jet development. For chemistry the constrained equilibrium model of Bilger and Stårner, [26] is adopted. In this model a pyrolysis flame sheet for the main fuel is included at $\xi_{ig} = \xi_{st} + 0.018$.

As a coupling submodel a presumed shape (β function) is used for the mixture fraction pdf $\tilde{P}_\xi$:

$$\tilde{P}_\xi(\zeta) = [\Gamma(a+b)/(\Gamma(a)\Gamma(b))] \times \zeta^{a-1}(1-\zeta)^{b-1}, \quad (1)$$

where the tilde denotes Favre averaging and Γ denotes the gamma function. First order closure is applied for chemistry by constructing modeled transport equations for $\tilde{\xi}$ and $\widetilde{\xi''^2}$. These in turn determine uniquely the mixture fraction pdf parameters a and b. The temperature pdf $\tilde{P}_T$ is then obtained [27] as

$$\tilde{P}_T(T) = \tilde{P}_\xi(\xi_1)/|dT/d\xi|_{\xi=\xi_1} + \tilde{P}_\xi(\xi_2)/|dT/d\xi|_{\xi=\xi_2} \quad (2)$$

because temperature is a double-valued function of mixture fraction, $T(\xi_1) = T(\xi_2)$. The calculations in Eq. 2 are performed numerically. The beta function representation of Eq. 1 poses certain limitations in the description of the physical processes occurring in the jet flame. It cannot handle an intermittency-induced delta function at $\xi = 0$ and at the same time a continuous distribution with a maximum in the range $0 < \xi < 1$, or zero contributions at both $\xi = 0$ and 1 and a continuous distribution with two local maxima in the range $0 < \xi < 1$. Bimodal pdf representations are thus impeded. Finally, although no intermittency was explicitly included in the mathematical model, the notion of intermittency is maintained throughout the next section. Furthermore, intermittency will be considered in the fluid mechanical rather than the thermo-

chemical context; it will thus indicate contributions from the secondary quiescent flow, whereas the interactions between the jet and annulus flows will retain a fully turbulent description. This approach is particularly useful in certain areas of the jet flame (in small x/d for example) where one of the preceding processes dominates. Nonadiabaticity was not included in the model because gas or soot radiation heat losses were negligible (temperature drop less than 15 K for $x/d < 66.7$).

RESULTS AND DISCUSSION

Figure 4 presents radial profiles of CARS measured and numerically predicted mean temperatures and rms temperature fluctuations, as well as thermocouple mean temperature data, for seven streamwise locations. Each CARS data point is the average of over 1000 measurements. This population yields a statistical confidence on the mean reduced temperatures ranging from 2 to 18 K whereas the statistical confidence on the rms temperature fluctuations is about 2.3% of their corresponding values. CARS measurements are acquired on both sides of the jet flame to properly determine the jet width and examine possible asymmetries. The radial traversing step ranged from 0.5 mm in the steep gradient parts of $x/d = 4.2$ to 3 mm at $x/d = 66.7$. The thermocouple radial traversing step ranged from 0.5 mm at $x/d = 4.2$ to 2 mm at $x/d = 41.7$.

Comparison with Thermocouple Measurements

We first compare CARS and thermocouple mean temperatures. The thermocouples [16] were of uncoated 50-μm-thick Pt/Rh(6%)-Pt/Rh(30%) with a bead diameter of 130 μm. Limitations arise due to chemical (catalytic), aerodynamic, and thermal effects. Thermal effects were accounted for by allowing for radiation and conduction heat losses. Conduction heat loss poses a difficulty at the lowest streamwise locations with steep temperature gradients across the thermocouple wires. Catalytic effects can become important in uncoated thermocouples and particularly in the fuel-rich flame parts leading sometimes [28] to substantial temperature overestimates; there is no evidence of this in the turbulent jet flame. Aerodynamic effects are difficult to characterize; nevertheless, care was taken in the thermocouple positioning to minimize flow field disturbances.

At the jet core and for $x/d \geq 16.7$ temperatures as measured by CARS are higher than those measured by thermocouples, by as much as 30 K. This can be attributed, as discussed in the Experimental section, to the CARS convolution effects in the fuel-rich areas. At $x/d = 4.2$ and 8.3, however, CARS core temperatures are lower by 60 and 100 K, respectively. A possible explanation is that the steeper gradients at the jet core of the lowest two streamwise locations lead to a spatial averaging-induced low-temperature biasing. This overtakes the milder high-temperature convolution biasing. Both CARS and thermocouple measurements show a small increase in mean peak temperature with increasing x/d, for $16.7 \leq x/d \leq 41.7$. In this region CARS mean peak temperatures increase from 1570 to 1620 K. CARS peak temperatures are higher by as much as 20 K than their thermocouple counterparts, for $x/d \geq 16.7$. For $x/d = 4.2$ and 8.3, however, CARS peak temperatures are lower by about 270 and 160 K, respectively. The last discrepancies are rather large and can be attributed to low-temperature biasing due to CARS-induced spatial averaging and to errors introduced during the thermocouple conduction correction. Both effects stem from the higher-temperature gradients encountered at the lowest streamwise distances. An additional factor is the relative coarse radial traversing steps (0.5 and 1 mm at $x/d = 4.2$ and 8.3, respectively) in both types of measurements. The same reason could possibly account for an observed asymmetry in the CARS and thermocouple temperature profiles at $x/d = 4.2$ and 8.3.

At the jet flanks CARS measurements are more susceptible to spatial averaging, leading to low-temperature biasing. A quantification of this biasing was performed in [22], by adopting a two-temperature fluid model within the CARS volume. The modeled CARS temperature exhibits a defect compared to the thermodynamic mean temperature that depends on

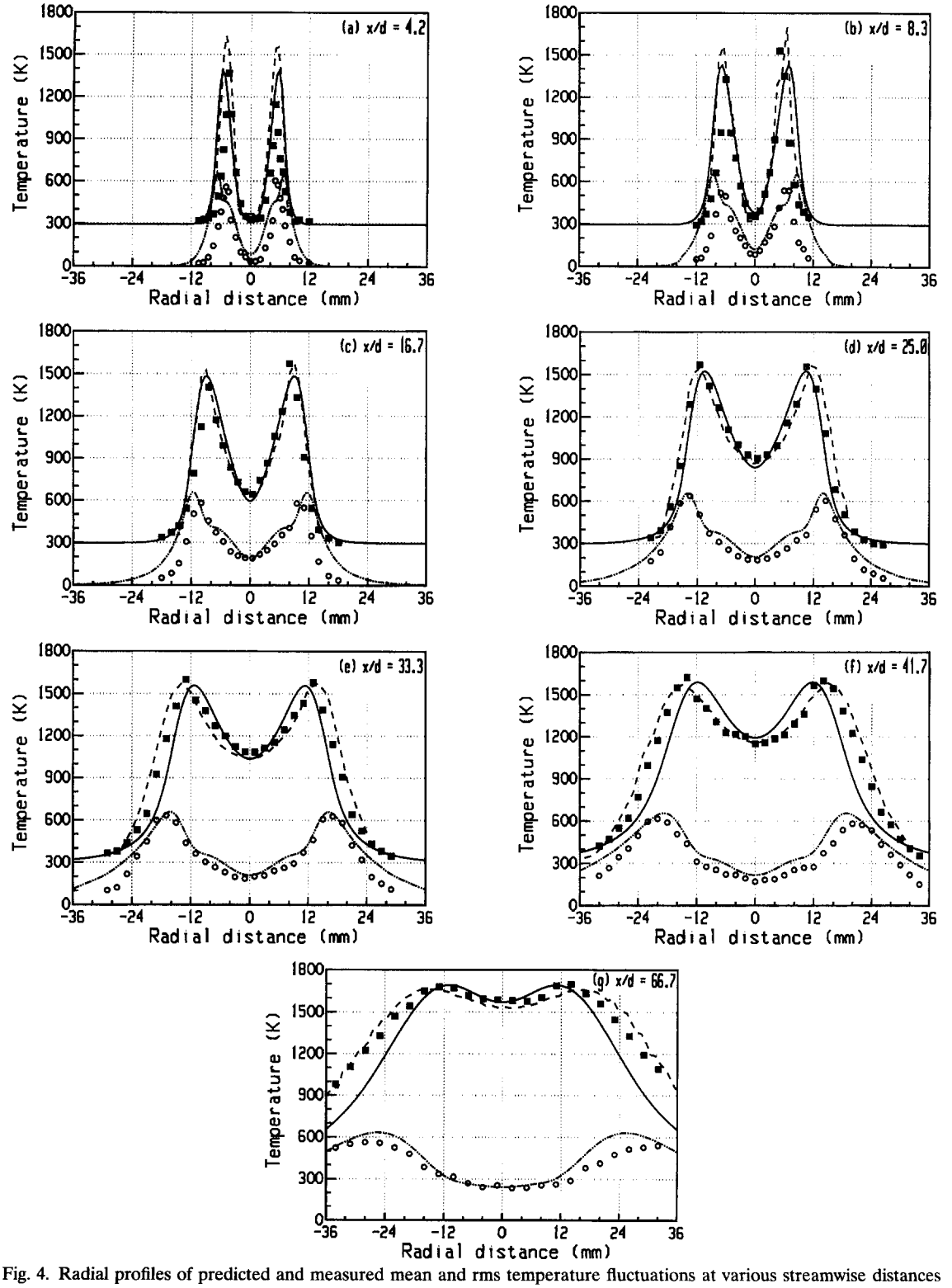

Fig. 4. Radial profiles of predicted and measured mean and rms temperature fluctuations at various streamwise distances x/d. Mean temperatures: CARS (divided boxes), thermocouple (dashed line), predictions (solid line); rms fluctuations: CARS (circles), predictions (dot-dash lines).

the chosen pair of low and high temperatures and the volume fraction occupied by each type of fluid. For a pair of fluids with temperatures of 600 and 2200 K, for example, the maximum defect can be as high as 300 K. Bradley et al. [29] corrected their single-temperature fit CARS pdfs (acquired in the reaction zone of a weakly turbulent premixed flame) using a two-fluid model avoiding a substantial (450-K) mean temperature underestimate. Such an approach was not necessary in this study, because both our spatial resolution (0.9 mm as opposed to 3 mm in [29]) and the strong turbulent fluctuations in the reaction zone location resulted in much lower temperature underestimates. When CARS and thermocouple data are compared in the steep gradient areas of the jet flanks, two factors must be considered. The first is the CARS-induced defect from the mean thermodynamic temperature described previously; the second is the difference in thermodynamic temperatures due to size disparity between the CARS probe volume (0.9 mm) and the thermocouple beads (0.13 mm). The relative weighting of the second factor is also expected to decrease with increasing x/d, as turbulent scales increase.

We can now attempt to assess the effects of spatial averaging for the lowest streamwise location $x/d = 4.2$. The maximum mean temperature gradient at the jet flanks calculated from Fig. 4a is about 600 K/mm, and certainly the instantaneous gradients can be much steeper. Following [22] we can estimate a maximum temperature defect of more than 200 K. In the jet flank areas mean temperatures as measured by CARS appear lower than those measured by thermocouples, by as much as 350 K. In the steep gradient areas the temperature statistics are not reliable except possibly around the centerline and we shall not elaborate on the $x/d = 4.2$ streamwise location. The steepest mean temperature gradients decrease rapidly as x/d increases; typical mean temperature gradients calculated from Fig. 4 are 400 ($x/d = 8.3$), 220 ($x/d = 25.0$), and 30 K/mm ($x/d = 66.7$). This leads to CARS mean temperatures that are lower than thermocouple temperatures by about 50–70 K in the jet flank areas, for all locations $x/d \geq 25$. Finally in the tails of the jet profiles ($T < 500$ K) and for $x/d \geq 16.7$ the agreement is very good, with the thermocouple measurements higher by about 25 K. For $x/d = 8.3$ the agreement is still good with thermocouple temperatures higher by about 80 K. Overall, the agreement between CARS and thermocouple measurements is excellent in the core region of the jet flames and very good in all other areas, at least for $x/d \geq 16.7$.

Comparison of CARS Measurements with Numerical Predictions

Two issues are of interest in comparing temperature profiles. The first is the model limitations near the burner, arising from the three dimensionality of the pilot flames: the flow is three-dimensional and nonisotropic and cannot be captured well by the axisymmetric k-ε model. The second issue is the underprediction of jet width spread rate [16]. These facets also have implications for the thermal jet profiles, as will be discussed subsequently.

The following comparisons refer to Favre-averaged predictions. There is no clear demarcation, however, as to the specific nature of the measurements (Favre or Reynolds averaged); as the density decreases, spatial averaging effects become more important, resulting in a low-temperature biasing that could mimic a Favre-averaged process. We first compare mean and rms temperature profiles at $x/d = 25$ (Fig. 4d)—a distance where the thermal jet width is well predicted. Predicted peak and centerline mean temperatures are lower than the CARS values by about 50 K. Except for the centerline region, core mean temperatures are overpredicted by about 50 K. Jet flank temperatures are underpredicted by as much as 80 K, partly due to slight jet width underprediction. Peak computed rms values are in very good agreement with the measurements (640 K). Predicted and measured peak rms fluctuations occur at radial locations corresponding to about 70% of the full height of the mean temperature profile, and this is also the case for all values of x/d. The predicted rms profile exhibits kinks at the radial locations of peak mean temperature for all streamwise distances $x/d \leq 41.7$. The measurements show milder kinks for $25 \leq x/d \leq 41.7$, which are more evi-

dent at $x/d = 41.7$ and 33.3. It is worth noting that kinks in the rms temperature radial profiles at the radial position of peak mean temperature have been observed to be even more pronounced, taking the form of local maxima, in the H_2 (Re = 8500) jet flame of Drake et al. [13] at their lowest streamwise location ($x/d = 10$), as well as in the CH_4/H_2 jet flame of Dibble and Hollenbach [12] at their highest streamwise location ($x/d = 110$), and also in a lower Reynolds number (Re = 4900) jet flame of our burner for $x/d \leq 25$.

At $x/d = 8.3$ and 16.7 (Fig. 4b and c, respectively) peak mean temperatures are underpredicted by about 100 K, whereas at all higher streamwise locations the underprediction is less than 50 K, becoming as low as 15 K at $x/d = 66.7$. Predicted and measured centerline mean temperatures are within 50 K (see also Table 1). The thermal jet width is overpredicted for $x/d \leq 16.7$ and underpredicted for $x/d \geq 25$. The jet width mismatch is primarily responsible for the substantial mean temperature discrepancies at the jet flanks (overprediction by about 400 K at $x/d = 8.3$ and underprediction by about 300 K for $x/d = 66.7$). When the pdf shapes will be compared in the next section, this mismatch will be accounted for by a rescaling of the predicted profiles. The predicted peak rms temperatures are nearly constant for $x/d \leq 41.7$ (655 K), with a somewhat lower value (630 K) at $x/d = 66.7$. The agreement with CARS measurements is very good (within 20 K) for $x/d \geq 25$, whereas for $x/d \leq 16.7$ predictions are higher by 50–100 K. Centerline rms temperatures are slightly overpredicted for $x/d \geq 16.7$ (agreement within 20 K), whereas at $x/d = 8.3$ the overprediction is about 40 K (see also Table 1). Additional factors contributing to the preceding differences are flame extinction (frequent in these low streamwise locations), strain-reduced flame temperatures, and incorrect turbulent mixing. The measured maximum rms temperature fluctuations in the CH_4 jet flames of Masri et al. [1, 2] were 658 K (very close to our measured value of 640 K). In the H_2/CH_4 flame of Dibble and Hollenbach [12] peak rms values were as high as 475 K. In the H_2 flame of Drake et al. [13], as well as in the lifted CH_4 flame of Stårner et al. [4], peak rms temperature fluctuations were as high as 750 K.

Overall, the predictions of peak mean temperatures and peak rms fluctuations are very good for $x/d \geq 16.7$ and fair for $x/d = 8.3$. Centerline mean temperatures and rms fluctuations are very well predicted at all streamwise distances. The jet width is overpredicted at $x/d = 8.3$, but its spread rate is underpredicted downstream, resulting in narrower temperature profiles for $x/d \geq 25$.

Comparison of Temperature pdf Shapes

Figures 5 to 10 present computed and CARS-measured temperature pdfs for six streamwise distances in the range $8.3 \leq x/d \leq 66.7$. The majority of the measured pdfs are constructed from 5000 measurements. The higher population gives a statistical confidence on the mean values better than ± 9 K. At $x/d = 25$ (Fig. 7), the jet width is well predicted. This streamwise location serves as a reference case for the introduction of key issues such as flame strain, extinction, turbulent mixing, and intermittency, which are relevant to all other locations. The

TABLE 1

Measured and Computed Centerline Temperature pdf Parameters.[a]

x/d	Mean		rms		Skewness		Kurtosis	
8.3	354	381	112	114	2.15	2.20	8.6	8.3
16.7	640	594	188	182	0.58	0.96	3.3	4.1
25.0	900	840	192	204	0.66	0.61	3.8	3.5
33.3	1080	1036	195	209	0.72	0.47	3.7	3.3
41.7	1150	1192	184	217	0.67	0.38	3.9	3.1
66.7	1578	1571	235	238	0.19	0.03	3.1	2.7

[a]The first column in each entry corresponds to CARS-measured pdfs.

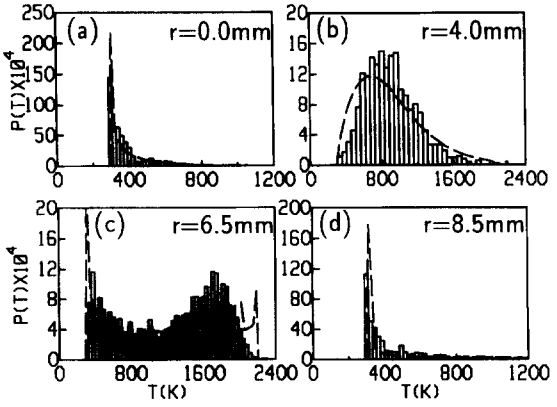

Fig. 5. Measured (open rectangles) and predicted (dashed lines) temperature pdfs at $x/d = 8.3$. (a), (c), and (d) were constructed from 5000 measurements and (b) was constructed from 1000.

radial distances for the predicted pdfs of Fig. 7 are shorter than the corresponding measured ones except near the centerline. As shown in Fig. 4b a small radial stretch (0.2–0.9 mm) of the predicted profiles is needed to attain a mean temperature profile match. This stretch also yields a better rms fluctuation profile match.

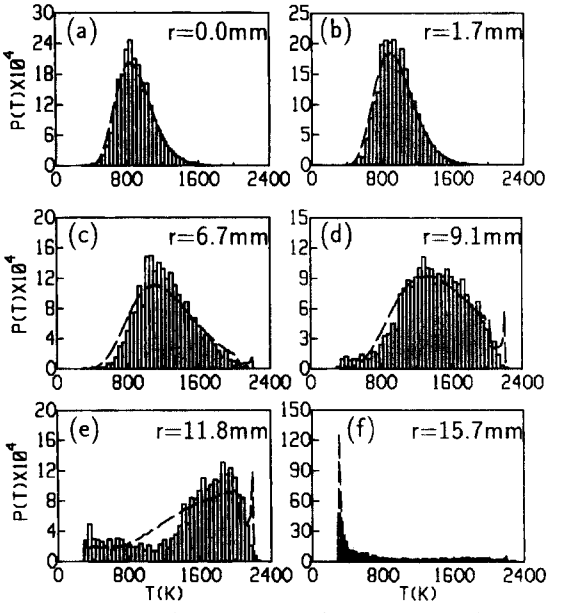

Fig. 7. Measured (open rectangles) and predicted (dashed lines) temperature pdfs at $x/d = 25$. All pdfs were constructed from 5000 measurements.

Figure 7a shows the centerline pdfs. The predicted pdf has been shifted by +60 K to account for the lower mean predicted temperature, because no radial stretch is possible at the centerline. A temperature shift of +50 K

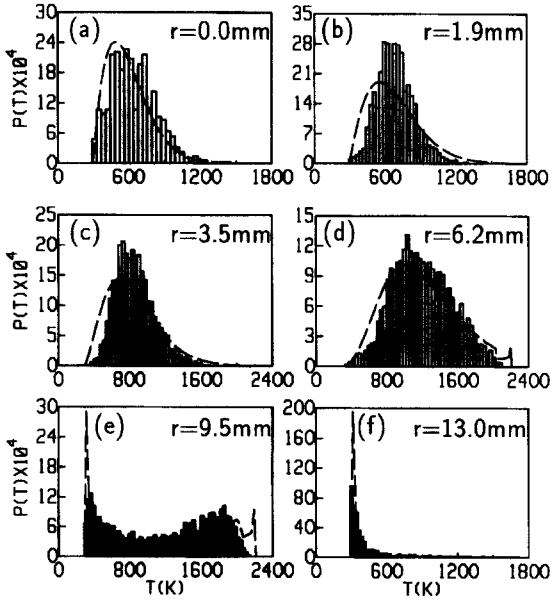

Fig. 6. Measured (open rectangles) and predicted (dashed lines) temperature pdfs at $x/d = 16.7$. (b)–(f) were constructed from 5000 measurements and (a) was constructed from 1000.

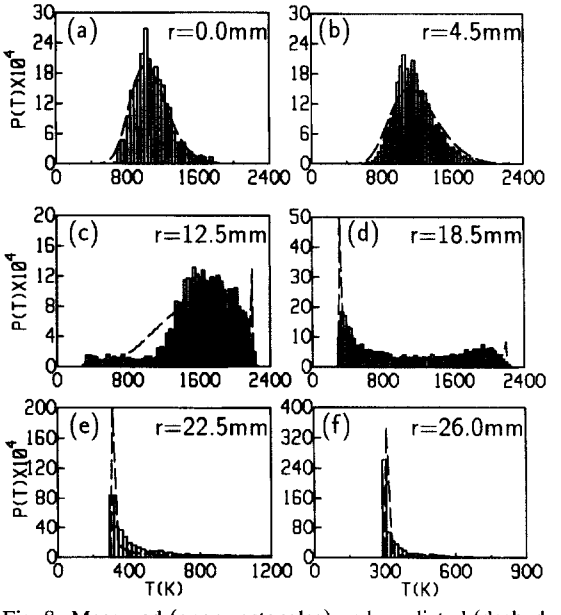

Fig. 8. Measured (open rectangles) and predicted (dashed lines) temperature pdfs at $x/d = 33.3$. (b)–(f) were constructed from 5000 measurements and (a) was constructed from 1000.

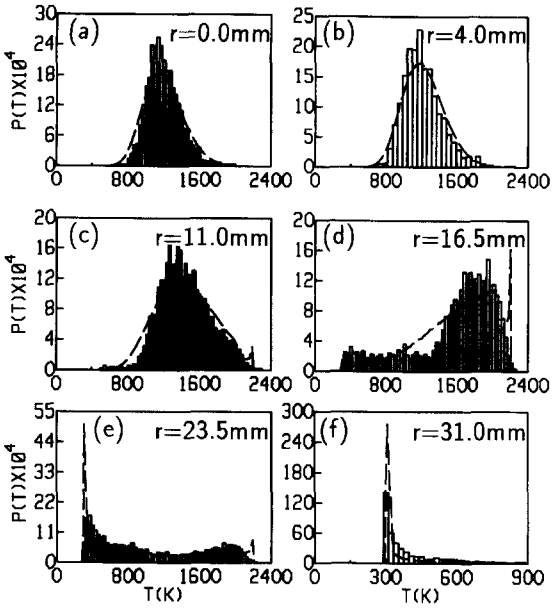

Fig. 9. Measured (open rectangles) and predicted (dashed lines) temperature pdfs at $x/d = 41.7$. (a) and (c)–(f) were constructed from 5000 measurements and (b) was constructed from 1000.

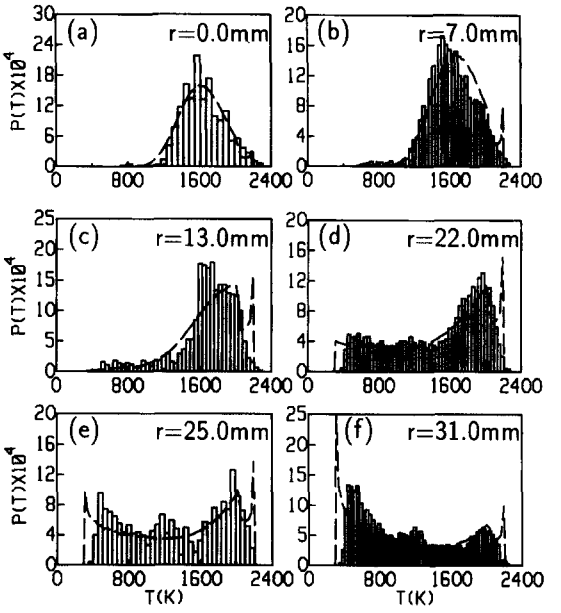

Fig. 10. Measured (open rectangles) and predicted (dashed lines) temperature pdfs at $x/d = 66.7$. (b), (d), and (f) were constructed from 5000 measurements; (a), (c), and (e) are constructed from 1000.

was also applied for the predicted pdf of Fig. 7b. The agreement between measured and predicted centerline pdfs is excellent. The predictions capture the mild skewness toward the hot side and only a narrow zone around the most probable temperature is underpredicted. Figure 7b–d are in the jet core region. Computed and measured pdfs become more asymmetric with increasing radial distance and their agreement is again very good. At various spatial locations the computed pdfs exhibit delta functions near the adiabatic flame temperature $T_f \approx 2200$ K (see, for example, Fig. 7d). This is because near the stoichiometric location ($\xi' \approx \xi_{st}$) Eq. 2 reduces to a single-valued function of ξ, $\tilde{P}_T[T(\xi')] = \tilde{P}_\xi(\xi')/|dT/d\xi|_{\xi=\xi'}$, with $|dT/d\xi|_{\xi=\xi'}$ becoming zero. The strength of this delta function in a temperature pdf constructed at a spatial location **x** shows the probability of the reaction zone ($\xi' \approx \xi_{st}$) to be located at **x**. Two comments can be made in this regard. First, CARS measurements clearly cannot resolve the reaction zone, and even if such a delta function existed, it would have smeared out in the measured pdfs. Second, at the streamwise location of Fig. 7, the strain rate is large and extinction is frequently encountered, as discussed in the Experimental section. Strain could thus redistribute the flame temperature population in a range of lower temperatures, and in the event of extinction to the lowest temperatures, result in a spread of the predicted spike. An equilibrium model, of course, cannot account for these effects. The discontinuity appearing in the predicted pdf shapes close to the flame temperature is due to the discontinuity in $dT/d\xi$ at the fuel decomposition flame sheet ($\xi = \xi_{ig}$). The low-temperature population (293–600 K) of Fig. 7d is underpredicted. It could be attributed to the inability of the model to account for extinction and/or to overprediction of turbulent mixing. These effects cannot be discriminated due to lack of simultaneous mixture fraction information.

Figure 7e is located at the peak mean temperature, which closely corresponds to the location of the average reaction zone. The entire allowable temperature domain from room temperature to flame temperature is now populated in both pdfs. The measured pdf approaches a bimodal shape, but the predicted

pdf shape, although qualitatively correct, does not capture this behaviour due to a population excess in the 900–1400-K range. It would thus appear that as bimodality is approached, the ability of a two-parameter β function pdf model to capture the details of the pdf shape is reduced. Figure 7f corresponds to the jet tail. The predicted room temperature delta function bears the contribution of two factors. The first is the initial ($x/d = 0$) pdf shape of $\tilde{P}_\xi$, which is a double delta function at $\xi = 0$ and $\xi = 1$. As $\tilde{P}_\xi$ evolves downstream, the areas of both delta functions are reduced through turbulent mixing. The second factor is the intermittency-induced delta function on $\tilde{P}_\xi$ at $\xi = 0$. Both pdf shapes of Fig. 7f are in good agreement; an exception is the predicted strength of the delta function at 293 K. The random error of ± 20 K in the cold parts of the jet could account to a large extent for the observed difference by redistributing the measured room temperature population fraction over a somewhat larger range. In addition, Favre averaging emphasizes the cold delta function contribution compared to Reynolds averaging (as also noted in [30]) and our measurements at such low temperatures are closer to Reynolds averaging. Another factor contributing to the discrepancy is the underprediction of turbulent mixing. The contribution from intermittency is not significant at $x/d = 25$, because turbulent eddies have not grown sufficiently to entrain secondary air flow. Overall the agreement between measured and predicted pdf shapes at $x/d = 25$ is impressive given the model limitations in both turbulence and chemistry. The agreement is particularly good in the jet core zone. Chemistry models have appeared [31] that close the mean reaction rates by assuming a joint Gaussian pdf for the temperature and species mass fractions. The marginal pdf of temperature is hence Gaussian and, as Fig. 7 suggests, this is consistent with our findings only around the centerline.

We further discuss pdf shapes at other streamwise locations, starting with the centerline pdfs. Table 1 provides the first four moments for the measured and computed centerline pdfs. The measured pdf at $x/d = 8.3$ is highly skewed, with a skewness of 2.15, but as x/d increases, the measured pdfs become more symmetric and reach a skewness of 0.19 at $x/d = 66.7$. The measured kurtosis falls from 8.6 at $x/d = 8.3$ to 3.1 at $x/d = 66.7$. The skewness and kurtosis for a Gaussian pdf are 0.0 and 3.0, respectively. It thus appears that measured pdfs approach a Gaussian shape with increasing x/d. There is debate [32] as to whether the joint thermochemical scalar pdf evolves to a Gaussian shape, at least for nonreacting cases. Predicted and measured pdf shapes at all other values of x/d exhibit the same good agreement with that of the reference case ($x/d = 25$) discussed previously. Figures 8–10 present temperature pdfs for $x/d \geq 33.3$. Radial distances have been stretched out by as much as 6.0 mm (Fig. 10f) to attain a thermal profile match. Centerline and core pdfs are again very well predicted, whereas measured pdfs at the peak mean temperature location (Figs. 8c and 9d) are nearly bimodal and not well reproduced by the predictions. In the upper parts of the jet flank locations (Figs. 8d, 9e, and 10e), measured pdfs are nearly uniform. At the jet tails the measured pdfs attain an almost triangular shape (Figs. 8e, f and 9f) with overprediction of the room temperature population. This suggests that the model could underpredict not only turbulent mixing, but also the intermittency factor, because at $x/d \geq 33.3$ turbulent eddies are large enough to entrain secondary flow in certain parts of the jet. Pdfs at the lowest streamwise distances $x/d = 8.3$ and 16.7 are presented in Figs. 5 and 6, respectively. Centerline measured and predicted pdfs at $x/d = 8.3$ (Fig. 5a) are in very good agreement with each other and nearly triangular in shape. The high temperature ($T > 2000$ K) population fraction measured at the jet flank locations of Figs. 6e and 5c is smaller than the corresponding fraction at the jet flanks of higher streamwise distances (see, for example, Figs. 8d, 9e, and 10f). Two possible reasons contribute to this. The first is the steeper temperature gradients at $x/d \leq 16.7$, leading to a more pronounced CARS spatial averaging which depletes the higher temperature population. The second is the increased strain rate which leads to strain-reduced flame temperatures and flame extinction—effects frequent at

these locations but not captured by a constrained equilibrium model.

CONCLUSIONS

Temperature fluctuations have been mapped in a turbulent natural gas-fueled piloted jet diffusion flame with a fuel jet exit Reynolds number of 9700. These were compared with thermocouple measurements and with the predictions of a numerical model employing a k-ε model for turbulence and a constrained equilibrium model for chemistry along with a presumed shape (β function) for the mixture fraction pdf. The key conclusions are as follows:

1. Comparison with thermocouple mean temperatures at $x/d \geq 16.7$ shows very good agreement (within 60 K) in regions of moderate temperature gradients (jet core). At the steeper temperature gradient jet flanks, however, spatial averaging leads to CARS mean temperatures lower than the corresponding thermocouple ones by 100 K at $x/d = 16.7$ and by as much as 50 K for $x/d \geq 33.3$. At $x/d = 8.3$, jet core temperatures are still in very good agreement (within 50 K) whereas for those at the peak and jet flank the agreement is fair (within 150 K).
2. CARS-measured peak mean temperatures are constant within 20 K around 1550 K in the range $8.3 \leq x/d \leq 41.7$ and they increase to 1700 K at $x/d = 66.7$. Peak measured temperature rms fluctuations are about 640 K and they occur at radial distances corresponding to approximately 70% of the full jet height, for all streamwise distances. Centerline rms temperature fluctuations are nearly constant (around 190 K) for $16.7 \leq x/d \leq 41.7$ and finally attain a value of 230 K at $x/d = 66.7$.
3. Comparisons of CARS-measured and numerically predicted radial temperature profiles show very good agreement between peak and centerline mean temperatures, as well as peak and centerline rms temperature fluctuations for streamwise distances $x/d \geq 16.7$, and fair for $x/d = 8.3$.
4. Measured centerline pdfs are nearly triangular at $x/d = 8.3$, becoming more symmetric as streamwise distance increases and finally evolving to a Gaussian shape as computed higher moments suggest. Pdf shape predictions at the centerline are in excellent agreement with the measurements.
5. Measured temperature pdfs exhibit a wide range of shapes. They are nearly symmetric at the jet core with their shape very well predicted by the model. Close to the average reaction zone location the measured pdfs are nearly bimodal and the agreement with predictions is only qualitative, primarily due to the inability of the beta function to represent bimodality. At the higher temperature parts of the jet flanks the measured pdfs can be nearly uniform, whereas at the jet tails they become triangular. In these regions pdf predictions are very good except for the room temperature zone. Chemistry models employing Gaussian joint pdfs for the thermochemical scalars are consistent with the measurements only in the narrow zone around the centerline and for $x/d \geq 16.7$.

JM was supported by the European Community under contract ERB4001GT930039. Additional funding for this research came from the Foundation for Fundamental Research of Matter (FOM).

REFERENCES

1. Masri, A. R., Bilger, R. W., and Dibble, R. W., *Combust. Flame* 71:245 (1988).
2. Masri, A. R., Bilger, R. W., and Dibble, R. W., *Combust. Flame* 73:261 (1988).
3. Stårner, S. H., Bilger, R. W., Dibble, R. W., and Barlow, R. S., *Combust. Flame* 83:63 (1991).
4. Stårner, S. H., Bilger, R. W., and Barlow, R. S., *Eighth Symposium on Turbulent Shear Flows*, Munich, Sept. 1991.
5. Barlow, R. S., and Carter, C. D., *Combust. Flame* 97:261 (1994).
6. Goss, L. P., Trump, D. D., Lynn, W. F., Chen, T. H., Schmoll, W. J., and Roquemore, W. M., *Rev. Sci. Instrum.* 60:638 (1989).
7. Stårner, S. H., Kelman, J. B., Masri, A. R., and Bilger, R. W., *Exp. Thermal Fluid Sci.* 9:119 (1994).
8. Schefer, R. W., Namazian, M., and Kelly, J., *Combust. Flame* 99:75 (1994).

9. Stårner, S. H., Bilger, R. W., Lyons, K. M., Frank, J. H., and Long, M. B., *Combust. Flame* 99:347 (1994).
10. Taran, J. P. E., *Fifth International Conference on Raman Spectroscopy*, 1975, pp. 695–706.
11. Eckbreth, A. C. *Laser Diagnostics for Combustion Temperature and Species*. Abacus Press, Cambridge, MA, 1988, p. 220.
12. Dibble, R. W., and Hollenbach, R. E., *Eighteenth Symposium (International) on Combustion*, The Combustion Institute, Pittsburgh, 1981, p. 1489.
13. Drake, M. C., Pitz, R. W., and Lapp, M., *Laser Measurements of Nonpremixed H_2-Air Flames for Assessment of Turbulent Combustion Models*, 22nd Aerospace Sciences Meeting, Reno, Nevada, AIAA Paper No. 84-0544, 1984.
14. Goss, L. P., Switzer, G. L., and Trump, D. D., *Temperature and Species Concentration Measurements in Turbulent Diffusion Flames by the CARS Technique*, 20th Aerospace Sciences Meeting, Orlando, Florida, AIAA Paper No. 82-0240, 1982.
15. Stårner, S. H., and Bilger, R. W., *Combust. Flame* 61:29 (1985).
16. Peeters, T. W. J., Stroomer, P. P. J., de Vries, J. E., Roekarts, D., and Hoogendoorn, C. J., *Twenty-Fifth Symposium (International) on Combustion*, The Combustion Institute, Pittsburgh, 1994, p. 1241.
17. Stroomer, P. P. J., *Turbulence and OH Structures in Flames*, Ph.D. Thesis, Dept. of Applied Physics, Delft University of Technology, 1995.
18. Peters, N., in *Lecture Notes in Physics* (M. D. Smooke, Ed). Springer-Verlag, Berlin, 1991, p. 48.
19. Eckbreth, A. C., *Appl. Phys. Lett.* 32:421 (1978).
20. Greenhalgh, D. A., *J. Raman Spectros.* 14:50 (1983).
21. Snelling, D. R., Smallwood, G. J., and Sawchuk, R. A., *Appl. Opt.* 28:3226 (1989).
22. Boquillon, J. P., Pealat, M., Bouchardy, P., Collin, G., Magre, P., and Taran, J. P., *Opt. Lett.* 13:722 (1988).
23. Hall, R. J., and Boedeker, L. R., *Appl. Opt.* 23:1340 (1984).
24. Bengtsson, P. E., Alden, M., Kroll, S., and Nilsson, D., *Combust. Flame* 82:199 (1990).
25. Brüggemann, D., and Heshe, S., *DACAPO-CARS Spectra Evaluation Code User's Guide*, ITLR, University of Stuttgart, 1993.
26. Bilger, R. W., and Stårner, S. H., *Combust. Flame* 51:155 (1983).
27. Williams, F. A., *Combustion Theory*. Benjamin/Cummings, Menlo Park, CA, 1985, p. 382.
28. Heitor, M. V., and Moreira, A. L. N., *Prog. Energy Combust. Sci.* 19:259 (1993).
29. Bradley, D., Lawes, M., Scott, M. J., Sheppard, G. W., Greenhalgh, D. A., and Porter, F. M., *Twenty-Fourth Symposium (International) on Combustion*, The Combustion Institute, Pittsburgh, 1992, p. 527.
30. Bilger, R. W., in *Turbulent Reacting Flows* (P. A. Libby and F. A. Williams, Eds.), Springer-Verlag, New York, 1980, p. 78.
31. Bockhorn, H. B., *Twenty-Second Symposium (International) on Combustion*, The Combustion Institute, Pittsburgh, 1988, p. 655.
32. Pope, S. B. *Prog. Energy Combust. Sci.* 11:119 (1985).

Received 3 November 1995